Scientific Reports

https://doi.org/10.1038/s41598-026-44065-8

Article in Press

Metal-displacement-derived silver nanoparticles for visible-light catalysis and TENG-enabled circuit integration

Received: 10 January 2026

Accepted: 9 March 2026

Published online: 23 March 2026

Cite this article as: Kandikonda R.K., Katru R., Madathil N. *et al.* Metal-displacement-derived silver nanoparticles for visible-light catalysis and TENG-enabled circuit integration. *Sci Rep* (2026). https://doi.org/10.1038/s41598-026-44065-8

Rajani Kumar Kandikonda, Rajesh Katru, Navaneeth Madathil, Nachimuthu Venkatesh, Raju Nagapuri, Rakesh Kumar Rajaboina, Haranath Divi, Chenna Reddy Mallu, Manikandan Dhayalan, Govindhasamy Murugadoss & Khanapuram Uday Kumar

Metal-Displacement-Derived Silver Nanoparticles for Visible-Light Catalysis and TENG-Enabled Circuit Integration

Rajani Kumar Kandikonda[a], Rajesh Katru[a], Navaneeth Madathil[a], Nachimuthu Venkatesh[b], Raju Nagapuri[c], Rakesh Kumar Rajaboina[a], Haranath Divi[a], Chenna Reddy Mallu[d]*, Manikandan Dhayalan*[e], Govindhasamy Murugadoss[b*,] Khanapuram Uday Kumar[a*]

[a]Energy Materials and Devices (EMD) Laboratory, Department of Physics, National Institute of Technology, Warangal 506004, Telangana, INDIA.

[b]Centre for Nanoscience and Nanotechnology, Sathyabama Institute of Science and Technology, Chennai-600 119, Tamil Nadu, INDIA.

[c]Department of Physics, Sreyas Institute of Engineering and Technology, Nagole, Hyderabad -500068, India

[d]Department of Chemistry, Freshman Engineering, Geethanjali College of Engineering and Technology, Hyderabad, Telangana, INDIA.

[e]College of Public Health Sciences, Chulalongkorn University, Bangkok, 10330, Thailand.

Corresponding Authors: manikandandhayalan88@gmail.com, murugadoss_g@yahoo.com, malluchennareddypvc@gmail.com, kanapuram.udaykumar@nitw.ac.in

Abstract

One of the main challenges in silver nanoparticle research is developing a quick, scalable, and environmentally friendly synthesis method that also produces stable particles suitable for various applications. To address this challenge, we propose an eco-friendly, simple and efficient approach using the metal-displacement process that enables room-temperature formation of uniformly dispersed and oxidation-resistant Ag NPs (25-50 nm). In this method, magnesium (Mg) acts as a sacrificial reductant, while tartaric acid serves as both a reducing agent and a capping agent. This novel magnesium-tartrate dual agent enables quick nucleation growth at room temperature, avoiding harsh chemicals,

and yields uniformly dispersed Ag NPs with strong oxidation resistance. The synthesised Ag NPs were characterised for structural, optical, and surface analyses, confirming the formation of pure metallic Ag^0 NPs with high stability due to tartarate chelation. These Ag NPs exhibited excellent photocatalytic activity, degrading 91.6% of Acid Yellow and 89.4% of Rose Bengal within 180 minutes under visible light, following first-order kinetics. Furthermore, the Ag NPs were formulated into a conductive ink capable of producing low-resistance printed tracks. The output of a triboelectric nanogenerator (TENG) was directly delivered to LEDs via these Ag-ink-printed pathways, enabling self-powered illumination of 240 LEDs. Overall, the present work provides a robust, scalable solution for multifunctional Ag NPs suitable for environmental remediation and next-generation printed electronics.

Keywords: Metal Nanoparticles, Silver, Metal-Displacement, Degradation, Conducting Ink, Organic Dyes.

1. Introduction:

Silver nanoparticles (Ag NPs) are widely used in catalysis, sensing, antimicrobial coatings, and printed electronics due to their size-dependent plasmonic, optical, and electronic properties [1]. A wide range of synthesis routes is employed that trade off Ag NPs size, shape control, scalability, cost, and environmental impact. Evaporation, condensation, laser ablation, and irradiation are top-down approaches that produce high-purity Ag NPs but require high energy and complex equipment, making large-scale production challenging [2,3]. Conversely, chemical reduction involves reducing agents for converting silver salts, usually $AgNO_3$, into metallic silver (Ag^0) [4]. These agents transfer electrons to initiate nucleation and nanoparticle growth. Typical reducing agents include ascorbic acid, gallic acid, ammonium formate, sodium borohydride, sodium citrate, polyol systems, and Tollens' reagent [5]. The characteristics of Ag NPs- particularly size, dispersity, and stability- are significantly influenced by the levels of reducing and stabilizing agents, as well as by reaction time, temperature, and pH [6,7]. Traditional methods like the Turkevich-Frens

citrate reduction and Tollens' process rely on exact reaction conditions to avoid aggregation and ensure uniform particle production [8–10]. However, these methods often use media with high ionic strength, toxic reagents, and generate waste, raising environmental and sustainability issues [11,12]. Photochemical, microwave, and sonochemical methods enable faster reduction and help to achieve uniform nucleation; nonetheless, they typically depend on polymeric stabilizers like PVP or PEG to prevent particles from coalescing [4,13,14]. The highly metallic and pure Ag NPs were reduced to Ag^{+} ions with modulating particle size by controlling the cathode current in electrochemical techniques [15,16].

A promising alternative is metal-displacement (galvanic replacement) synthesis, an eco-friendly redox-driven method capable of forming metallic silver at ambient conditions [17,18][19]. For example, Zozolya et al. demonstrated that sonogalvanic reduction of magnesium (Mg) to Ag could yield highly crystalline Ag nanoparticles within minutes [20]. Nevertheless, rapid reaction kinetics and the formation of metal-hydroxide by-products may affect uniformity and stability unless surface modifiers are used. The benefits and drawbacks of each method show that no single approach is superior across all criteria; rather, one must consider control, scalability, and sustainability when synthesizing Ag nanoparticles. This research gap underscores the need for a synergistic reductant-capping system that enables rapid, room-temperature synthesis without compromising nanoparticle stability or multifunctionality.

To address this challenge, the present work employs Mg-induced metal displacement combined with tartaric acid functioning as both a reducing and capping agent, a pairing that is rarely reported. The strong redox driving force of magnesium enables synergistic acceleration of the reduction process, improved kinetics, and obviates the need for harsh reducing agents. Simultaneously, tartaric acid regulates the particle growth and forms a robust chelating shell through its carboxylate and hydroxyl groups. This dual mechanism produces uniformly distributed Ag NPs that exhibit a clear surface plasmon resonance in the visible range

and have outstanding resistance to oxidation, effectively overcoming a key limitation of many galvanic and green synthesis techniques.

The present approach effectively integrates the rapid, straightforward metal-displacement method with tartaric acid's capping properties, yielding oxidation-resistant Ag NPs (25–50 nm) that retain their localized surface plasmon resonance (LSPR) signature even after prolonged air exposure. The Ag NPs exhibited excellent visible photocatalytic degradation efficiencies- 91.6% for Acid Yellow (AY) and 89.4% for Rose Bengal (RB) within 180 minutes- and rate constants of 0.029 min^{-1} and 0.025 min^{-1}. The nanoparticles were further formulated into a conductive ink that generated low-resistance printed tracks on non-conducting surfaces. These tracks were used as conducting tracks to integrate triboelectric nanogenerator (TENG) output with series-connected LEDs and to illuminate LEDs with TENG. Compared with the existing literature, this method achieves similar or superior activity while maintaining a sustainable, low-toxicity synthesis process, marking a significant advancement in environmentally friendly nanomaterial production.

2. EXPERIMENTAL METHODS

2.1. Materials & Methods

All chemical reagents, including silver nitrate ($AgNO_3$) and tartaric acid, were obtained from Merck and Sigma-Aldrich, and used as received. All the chemicals used were of the highest purity available. Ultrapure water was used for all the experiments (DM water).

2.2. Metal displacement synthesis of Silver nanoparticles

Tartaric acid (100 g) is mixed with 100 mL of DM water to obtain a tartaric solution. The pH of the solution was recorded as 2.67. The extract was used as obtained in all the experiments unless otherwise stated. Analytical-grade crystalline silver nitrate ($AgNO_3$, Merck) was used as received without further purification, is mixed with 100 ml of DM water to

obtain a tartaric solution and is stirred for 30 minutes [19]. The solution pH is checked, and this is the determining process parameter for size and purity. The pH of the solution was increased from 3.8 to 4.0. Subsequently, the solution is filtered for any undissolved raw materials. The filtered solution is introduced into the reaction chamber to add the Magnesium scrap, and the mixture is then placed in an ultrasonic bath for 15 minutes. The reaction was exothermic, and the solution temperature increased slightly. After 30 minutes, the reaction powder was collected at the bottom and filtered. This silver nanopowder was washed several times with DM water to remove contaminants. A flowchart of the metal-displacement synthesis is shown in **Figure 1.**

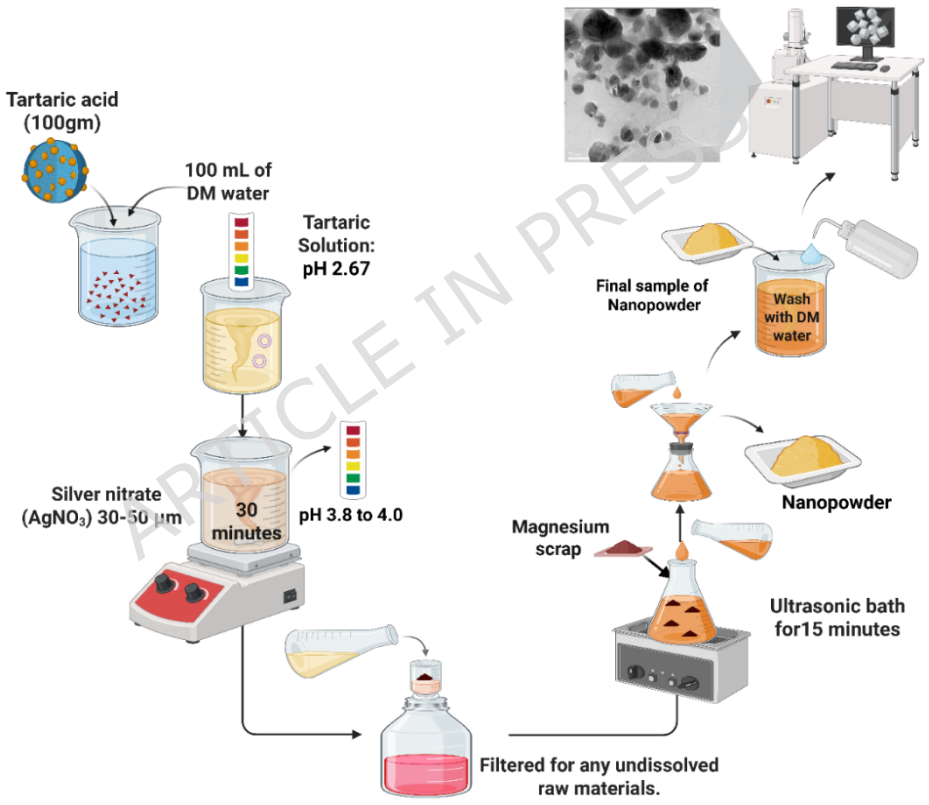

Figure 1: A flowchart of metal displacement synthesis of silver nanoparticles**.**

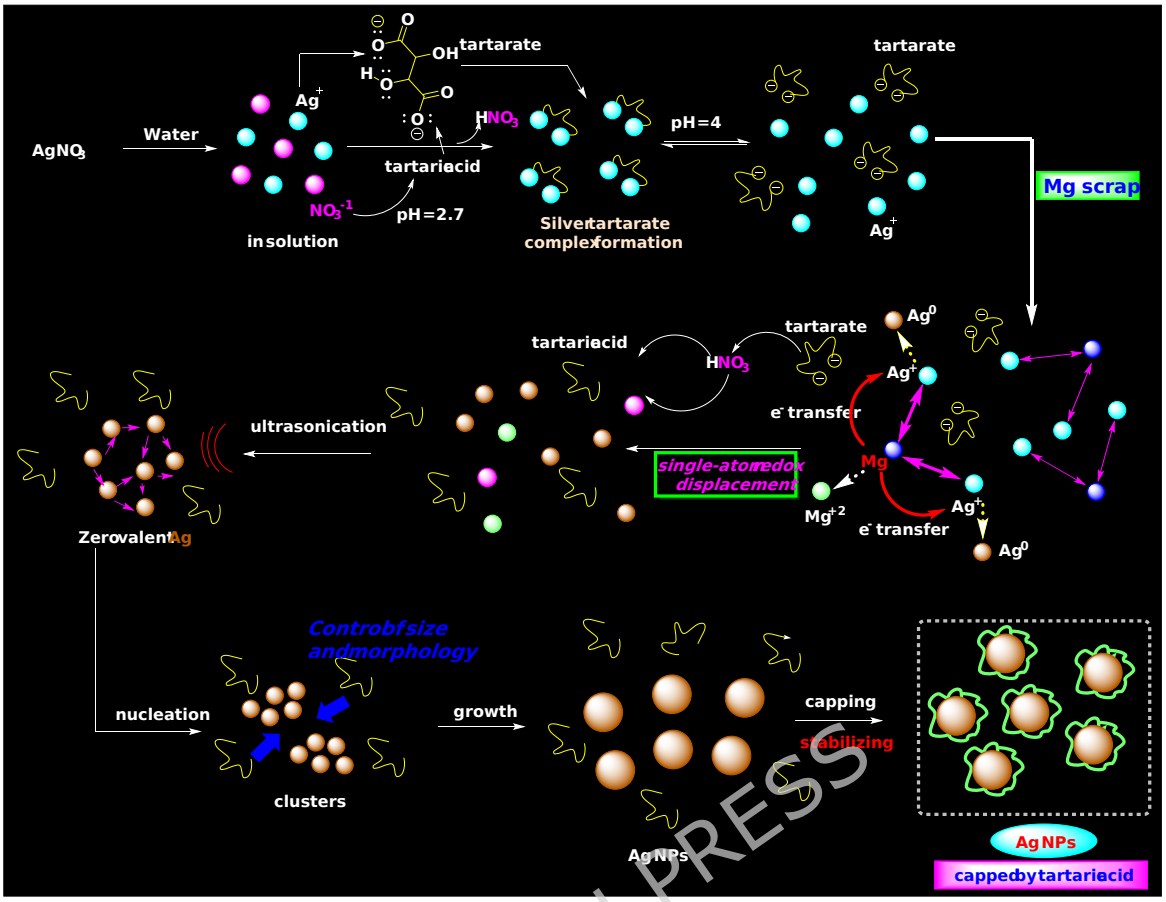

Figure 2: Mechanism illustration of the Ag NPs synthesis method.

The formation of silver metal nanoparticles from $AgNO_3$ in the presence of tartaric acid via single-atom redox metal replacement with Mg scrap is illustrated in **Figure 2**. Initially, $AgNO_3$ dissociates in water to produce Ag^+ and NO_3^- ions. The NO_3^- ions react with tartaric acid to form tartrate ions, which then bind with Ag^+ ions to produce a silver tartrate complex (**Figure 2**). Each tartrate ion coordinates to two silver ions, facilitating a single-atom redox-displacement reaction upon treatment with Mg scrap. This process involves the transfer of two electrons from one Mg (depicted in blue in **Figure 2**) to two Ag^+ ions (depicted in orange), resulting in Mg^{2+} (depicted in green) and two Ag^0 atoms [21,22]. The tartrate ions are subsequently released and can be regenerated by reacting with HNO_3, producing tartaric acid and NO_3^-. The high solubility of Mg^{2+} and NO_3^- in water facilitates the purification of the resulting Ag nanoparticles [23]. Nucleation of zero-valent silver under ultrasonication yields small clusters that gradually grow into Ag nanoparticles [24,25].

These nanoparticles are stabilised and capped with tartaric acid, ensuring their stability [26]. The crucial step in this process is the single-atom redox displacement of Ag^{+} by Mg metal ions. To our knowledge, this novel step has not been reported or proposed previously.

2.3. Characterization of Ag-NPs:

The crystalline nature and crystalline size of the synthesised Ag NPs was confirmed by X-ray Powder Diffraction (XRD) measurements, using an Anton Paar diffractometer (model XRDYNAMIC500) with a 2θ range of 30° to 80°. To identify vibrational modes of Ag NPs, a Raman spectrophotometer (RAMAN 785ER) was used. Diffusive reflectance spectrum used for recording the signature peaks of Ag NPs using the Carry 5000 instrument in the 200 nm-800 nm wavelength region. Similarly, absorption spectra were recorded within the 200 nm to 800 nm wavelength range. X-ray photoelectron spectroscopy was employed to ascertain the chemical state and valence states of the Ag NPs using Thermo Fisher Scientific, USA. The surface morphology and structural elemental composition of Ag NPs were analysed using field-emission scanning electron microscopy (FE-SEM, JEOL JSM IT-800), equipped with electron-dispersive spectroscopy (EDS), and Transmission electron microscopy (TEM), JEOL 2000 plus.

2.4. Photocatalytic Study

Photodegradation of organic dyes, such as Acid Yellow (AY) and Rose Bengal (RB), involves addressing these carcinogenic substances that are detrimental to the environment [27,28]. To decompose the dye molecules and mitigate their toxicity, a photocatalytic degradation process employing Ag NPs has been selected. In this experimental procedure, 25 mg of the synthesised catalysts was dissolved in 50 mL of dye solution. Subsequently, the catalyst-containing dye solution was exposed to visible light in a photoreactor for 3 hours. The photocatalytic experiments were carried out using a 500 W tungsten lamp as the visible-light source. The emission range of the tungsten lamp predominantly

covers the visible region (≈400–700 nm). Throughout the illumination process, 1.5 mL aliquots of the dye solution were collected at predetermined intervals for intensity measurement using a UV-visible spectrophotometer. The maximum absorbance wavelengths for AY and RB are 435 nm and 545 nm, respectively. The formula for calculating the degradation efficiency is as follows [27].

$$\text{Degradation efficiency (\%)} = \frac{C_0 - C}{C_0} \times 100 \quad (1)$$

Where C_0 and C are the initial and variable intensities of the dye molecules, respectively [27]. The treated sample was centrifuged following the first cycle to conclude the stability study, subsequently cleaned with acetone and water, and dried at 80 °c. Additionally, to ascertain the actual depolluting rate, a first-order kinetic analysis was performed.

$$-\ln\left(\frac{c}{c_0}\right) = kt \quad (2)$$

where k (min^{-1}) is the rate of reaction constant and t (min) is time. The photocatalytic research was conducted in a visible-light photoreactor, and light intensity was measured with a Digital Lux meter [29]. As a result, the average light intensity was 0.80 × 10^5 lux (6.67 kW/m^2), computed at 30-minute intervals.

3. Results & Discussion:

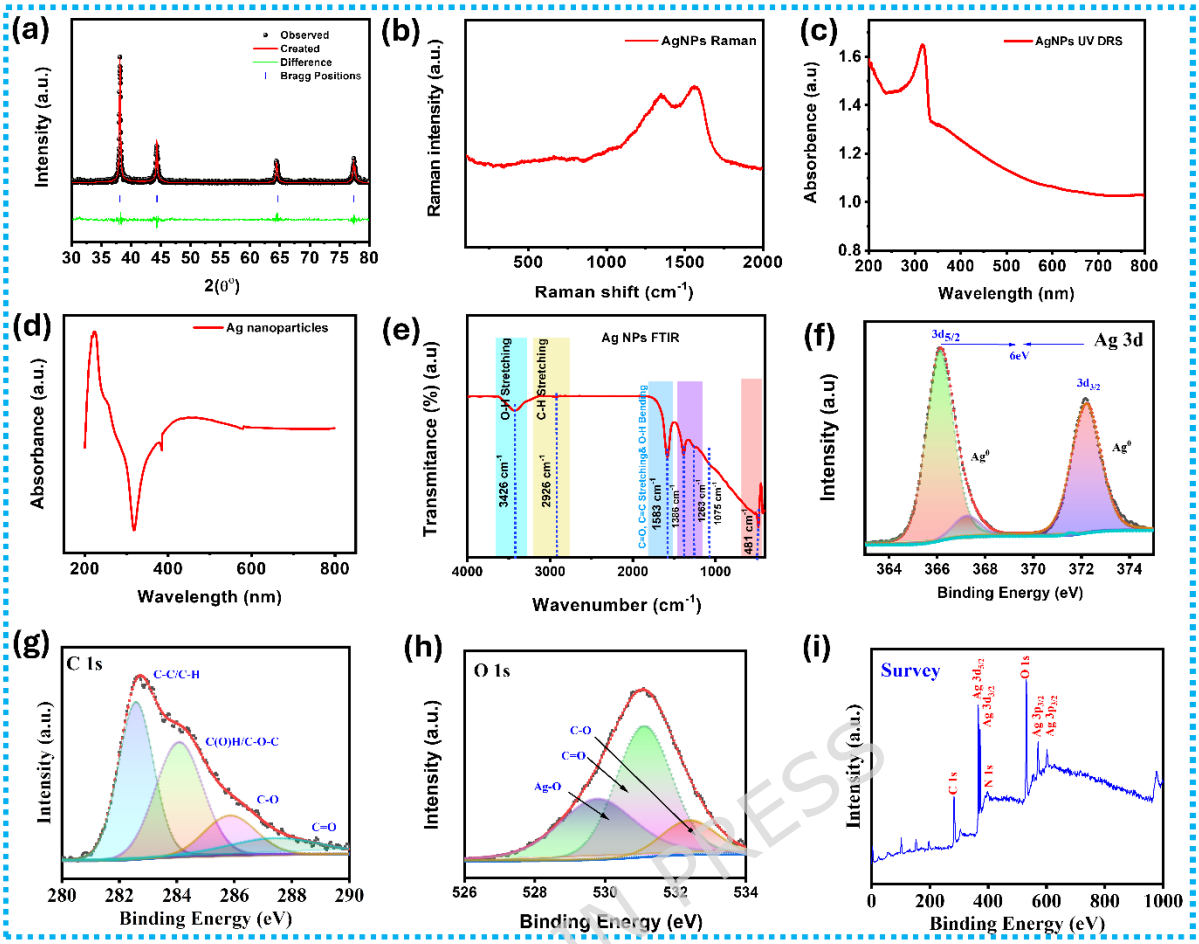

Figure 3: (a) XRD pattern of Ag NPs powder and retevield analysis, (b) Raman spectra, (c) UV-Diffusive Reflectance spectra, (d) UV-absorption spectra, (e) FTIR spectra, (f) XPS spectra of Ag-3d, C-1s, O-1s, and survey spectrum of Ag NPs.

The XRD analysis of the synthesized Ag NPs reveals a face-centred cubic (FCC) structure, consistent with the standard JCPDS data (# 04-0783) (shown in **Figure 3a**). The diffraction peaks at 38.2°, 44.4°, 64.7°, and 77.7° correspond to the (111), (200), (220), and (311) planes, respectively, indicating a high degree of crystallinity and confirming the formation of Ag^0 [30,31]. Rietveld refinement calculation yielded a lattice constant (a) of 4.08 Å, which is in good agreement with the reported value [15,32]. The average crystallite size, estimated using the Debye-Scherrer formula, is around 27.6 nm. Compared to reported literature, Ag NPs synthesis via chemical reduction, photochemical, and biosynthetic methods, the metal-

displacement method yields highly crystallised domains with well-developed crystallite size, with minimal macrostrain and almost no sign of oxidation. The sharp and intense peak of the (111) plane signifies the highly ordered preferential orientation of FCC domains, which are advantageous for surface plasmon resonance and photocatalytic activity [33,34]. The absence of impurity peaks confirms the nanoparticles' pristine phase, suggesting that the tartaric acid reduction method employed in this study is effective for producing pure Ag NPs.

Raman spectroscopic analysis confirmed the phase purity and metallic nature of Ag NPs (**Figure 3b**). The two major broad peaks at 1350 cm^{-1} and 1580 cm^{-1} correspond to the induced D band and the graphitic D band, which arise due to the tartaric acid reducing agent or trace adsorbed carbon. This feature is common in noble metal nanoparticles [35]. Importantly, no major Ag_2O or AgO stretching bonds were detected in the 430-450 cm^{-1}. Notably, $AgNO_3$ exhibits a significant and distinct $\nu_1(NO_3^-)$ mode around 1045 cm^{-1}, which is also not observed, indicating the formation of pure Ag^0 metallic nanoparticle [36,37]. Further, UV-Vis diffusive reflective spectroscopic analysis was performed, and the primary plasmonic resonance peak was observed at 317 nm (shown in **Figure 3c**). This peak could be attributed to the interband transition of metallic silver (4d→5sp) [38,39]. This peak signifies the fingerprint feature of Ag^0 and arises due to the electron excitation within the conduction band [40]. **Figure 3d** shows the UV-Vis transmission spectra of Ag NPs [39]. The absence of other oxidation and $AgNO_3$ peaks can also be observed from the DRS spectrum, further confirming the pure metallic nature of Ag NPs [41]. A broad decaying tail beyond 350 nm, associated with dense or aggregated Ag NPs, is a common feature of metal nanoparticles.

As illustrated in **Figure 3d,** the UV-Vis transmission spectrum of Ag NPs has three salient regions. The first region, around 250 nm, is due to the electron absorption dominated by $\pi \rightarrow \pi^*$transition of the capping agent, such as tartaric acid and the Ag interband continuum [42,43]. Second, a pronounced trough at around 330 nm, which is due to the gap between UV

interband absorption and plasmonic response. Notably, at 302 nm, there is no $AgNO_3$ peak observed [44]. A third feature corresponds to LSPR of metallic Ag NPs, which appears to broad plateau around 430-500 nm [6].

The as-synthesized Ag NPs were analysed using FTIR spectroscopy in the 400-4000 cm^{-1} spectral range to assess the chemical bonding through infrared light interaction. As shown in **Figure 3e**, the absorption bands were observed at 3426, 2926, 1583, 1386, 1263, 1075, and 502 cm^{-1}. The band at 3426 cm^{-1} corresponds to O-H stretching vibrations, and 2926 cm^{-1} is assigned for C-H stretching vibrations [45]. The 1583 cm^{-1} band and 1386 cm^{-1} are linked to C=O and C=C stretching vibrations and C-H bending of tartaric acid [46,47]. The band at 1263 cm^{-1} is due to C-N stretching of amine groups, and the 1075 cm^{-1} band corresponds to C-N stretching of protein groups [48]. The prominent 550 cm^{-1} band usually attributed to Ag_2O is absent, suggesting the metallic nature of Ag NPs [49].

X-ray photoelectron spectroscopy studies have been performed to analyse the chemical composition of the silver nanoparticles. The survey spectrum, as shown in the figure, indicates the presence of C and O, originating from the reference molecular stabilizer and absorbed gases, respectively. The binding energies at 366 and 372 eV correspond to the spin-orbit splitting of Ag $3d_{5/2}$ and Ag $3d_{3/2}$, respectively, and align well with the literature (as shown in **Figure 3f**). Notably, the energy difference between the Ag 3d peaks confirms the presence of metallic silver (Ag^0). Additionally, the satellite peak at 367.4 eV serves as a characteristic indicator of the Ag^0 state.is the fingerprint of the Ag^0 state [50,51]. The high-resolution spectrum of the C 1s deconvolutes into four peaks at 282.5, 284.05, 286.05, and 287.7 eV (as shown in **Figure 3g**). These peaks are assigned to the following functional bonds: C-C/C-H, C-OH/C-O-C, C-O, and C=O, respectively [52,53]. As illustrated in **Figure 3h**, the high-resolution O 1s spectrum shows three peaks at binding energies of 529.7, 531.1, and 532.3 eV. The first peak at 529.7 eV corresponds to atomic oxygen bonded to ionic Ag-O. The second peak at 531.1 eV indicates oxygen atoms diffusing into the bulk of Ag. Additionally, based on previous literature, O 1s peaks

with binding energies above 532.1 eV are associated with carbon-containing intermediates. The final peak at 532.3 eV represents residual oxygen (O res) within the silver metal lattice [54]. As shown **in Figure 3i,** the wide-scan spectrum shows only Ag, C, and O signals, consistent with metallic Ag nanoparticles capped by tartaric acid-derived species.

The surface morphology, shape, and size of the synthesized Ag nanoparticles were examined using FESEM (shown in **Figure 4(a, b)**). The images reveal predominantly spherical to slightly oval nanoparticles with a relatively narrow size range of ~20-35 nm, forming secondary agglomerated clusters of approximately ~45 nm. These clusters are composed of uniformly distributed primary Ag NPs, indicating controlled nucleation and growth during the metal-displacement process. The particles display clean surfaces without observable byproducts or irregular morphologies. The EDX spectrum (Figure 4c) shows a single, intense Ag signal with no detectable Mg or organic residues, confirming the high elemental purity of the synthesized Ag NPs.

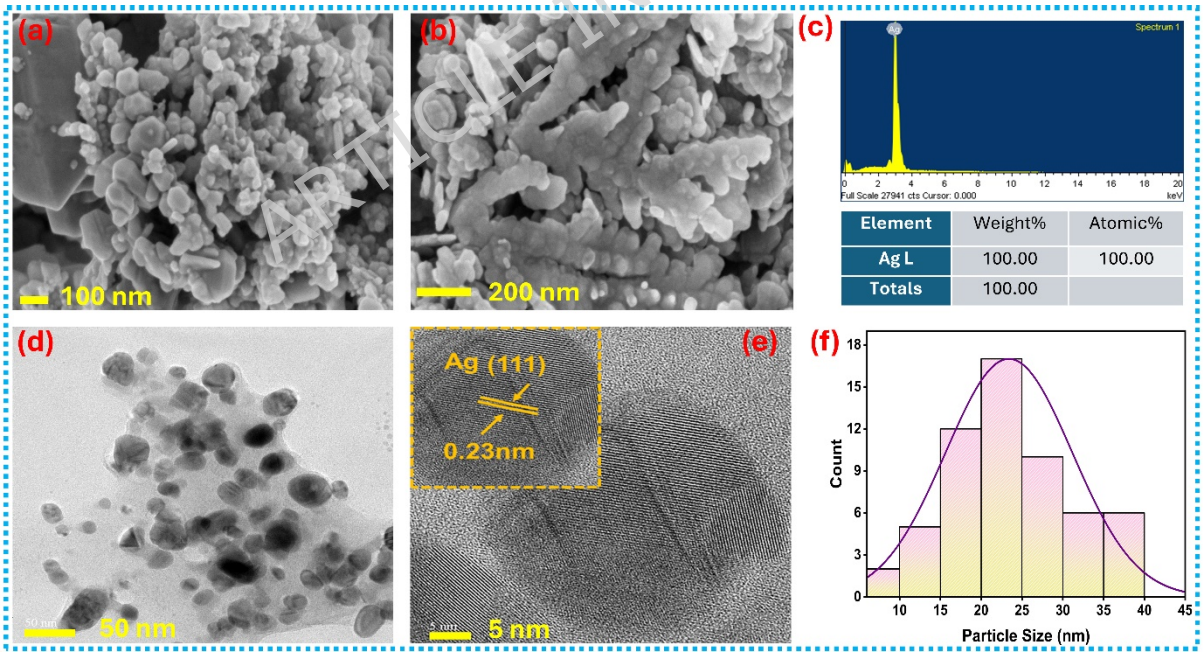

Figure 4: (a-b)FESEM images of Ag NPs and (c) EDX spectrum, (d-f) TEM micrograph, lattice spacing of Ag (111) plane and particle size histogram, respectively.

TEM micrographs (**Figure 4(d, e)**) show that the synthesized Ag nanoparticles are mainly spherical or slightly capsule-shaped, with a narrow size distribution and consistent morphology. The particles are evenly dispersed, with no sign of significant agglomeration, demonstrating effective stabilization by the tartaric acid capping layer. Most nanoparticles are in the 15-25 nm size range, with an average diameter of around 20 nm, as measured using ImageJ and illustrated in the particle size histogram (**Figure 4f**). The uniform contrast and distinct particle edges further confirm the formation of well-defined, nanoscale Ag NPs. The high-resolution TEM image (**Figure 4e**) reveals clear lattice fringes, indicating their crystalline structure. In conclusion, material characterisation confirms that the synthesised Ag NPs are pure, crystalline, oxidation-resistant, and uniformly dispersed. The Mg-tartrate system ensures controlled growth and strong surface stability. These properties demonstrate the potential of the Ag NPs for multifunctional uses. In the following sections, we assess their practical application in photocatalytic dye degradation and the fabrication of conductive ink tracks for electronic integration.

4. Photocatalytic activity of prepared Ag NPs

The photocatalytic performance and efficiency are primarily determined by a narrow bandgap for visible light absorption, adjustable electronic properties, and the generation of reactive oxygen species (ROS) through the combination of catalytic components. This present study investigates the photocatalytic potential of metallic Ag NPs, for the degradation of organic pollutants under visible light irradiation. Ag NPs serve as potent photocatalysts by augmenting visible-light harvesting, improving charge separation, and accelerating redox reactions, thereby rendering them highly effective for environmental remediation applications. Silver nanoparticles possess a higher surface-to-volume ratio, exposing more active sites for dye adsorption and subsequent reactions.

Figure 5(a, b) displays the UV-Vis spectra of AY dye following 180 minutes of catalytic treatment. A progressive decrease in the primary absorption peaks was observed, signifying the disintegration of essential chromophore groups responsible for the dye's coloration. The degradation efficiencies of AY by Ag NPs were recorded as 91.61%, respectively. These results underscore the superior photocatalytic performance of Ag NPs. The efficiency plot (C/C_0) for the AY and RB dye solutions is depicted in Figures **5(c, d).** The plot illustrates the degradation capability of the Ag NPs, which exhibited the highest degrading efficiency. **Figure 5(e)** clearly presents the kinetic analysis of the degradation process, confirming that it adheres to first-order kinetics. The rate constant for Ag NPs against AY dye was calculated as 0.029/min, respectively. Similarly, the photocatalytic efficacy of the prepared Ag NPs was evaluated against the RB dye solution. Under identical conditions, the degradation efficiency of the Ag NPs was 89.4%, and the rate constant against RB dye was 0.025/min, respectively.

Upon exposure to visible light, photons are absorbed by the photoactive catalyst, resulting in the generation of electron-hole pairs that serve as charge carriers. These carriers promote the formation of ROS, which are crucial to the photodegradation process. Generally, three types of ROS are produced, and it is imperative to identify and regulate the principal ROS responsible for the degradation mechanism. Scavenger experiments were performed to elucidate the photodegradation pathway of dyes utilising the Ag NPs catalyst, thereby offering valuable insights into the specific ROS involved and their respective roles in the degradation process. The scavenger reagents employed include Ethylenediaminetetraacetic acid (EDTA), methanol, and p-benzoquinone (BQ), which serve as h+ scavengers, ·OH scavengers, and $O_2{\cdot}^-$ scavengers, respectively [55]. The reagent was formulated to inhibit the activity of h^+, ·OH, and $O_2{\cdot}^-$. **Figure 6a** depicts the percentage degradation observed with various scavengers. The scavenger investigations demonstrated that the addition of EDTA and methanol markedly reduced the degradation efficiency of both dyes, thereby signalling their involvement in quenching

specific reactive species during the photodegradation process. The structure and morphology of the catalyst are crucial factors that affect its performance under visible-light illumination. Moreover, the reusability of the Ag NPs catalyst was examined over five successive cycles, as illustrated in **Figure 6b**, confirming its stability and demonstrating its potential for application in wastewater treatment.

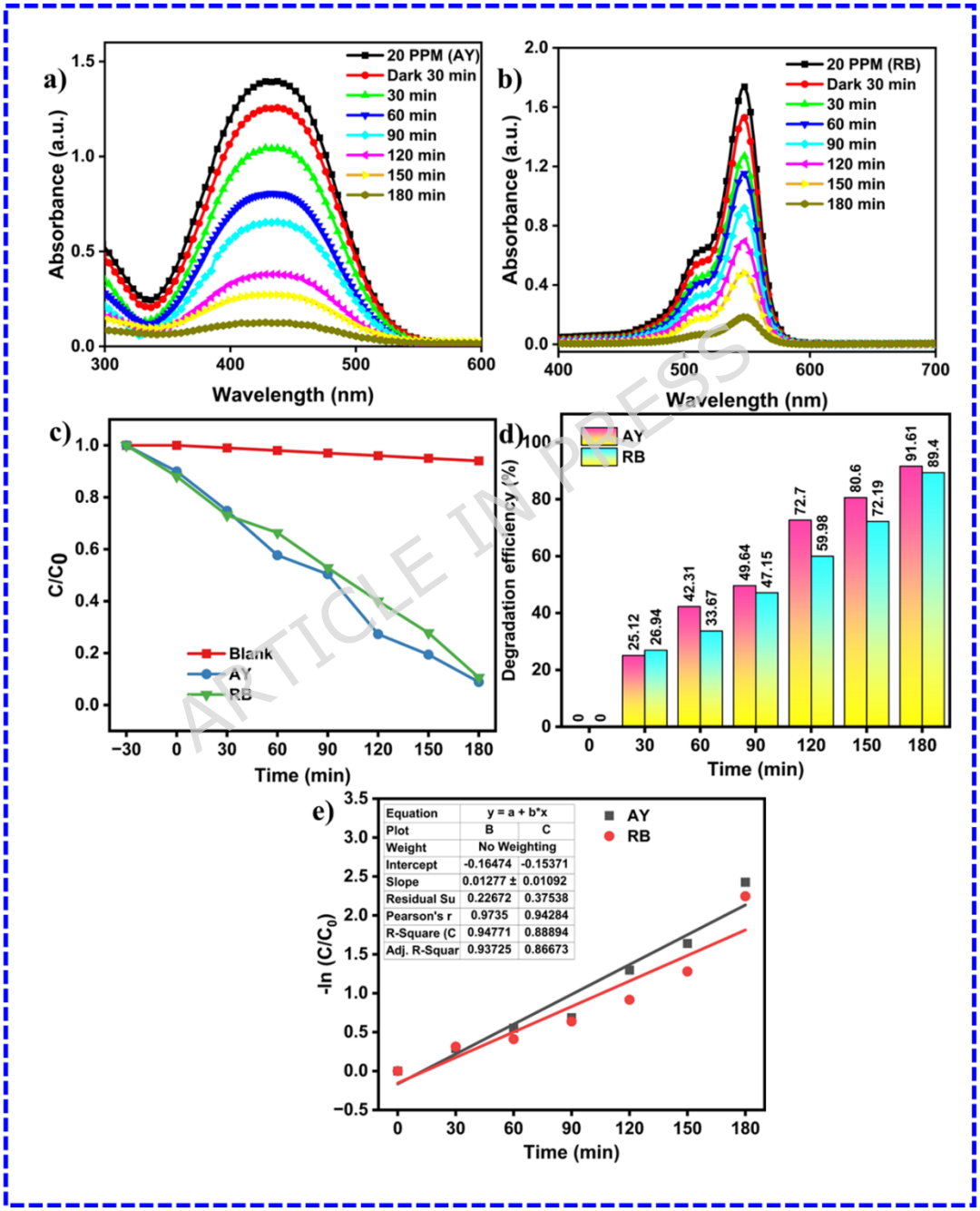

Figure 5: Photocatalytic degradation by Ag NPs (a) AY, (b) RB, (c) efficiency plot (C/C_0), (d) Degradation efficiency, and (e) degradation kinetic study of AY and RB dye.

The photocatalytic mechanisms are as mentioned below,

(i) Production of excitons

Silver (Ag) NPs + hν → h^+ (VB) + e^- (CB)

(3)

(ii) Hydroxyl Radicals Generation

$OH^- + h^+ \rightarrow OH\cdot$

(4)

$H_2O + h^+ \rightarrow OH\cdot + H^+$

(5)

(iii) Superoxide radicals Generation

$O_2 + e^- \rightarrow O_2\cdot^-$

(6)

(iv) Degradation of dye molecules

AY and RB dyes + $OH\cdot + O_2\cdot^-$ → Degradation products

(7)

Ag nanoparticles exhibit a pronounced synergic effect on the photocatalytic degradation of RB and AY dyes. Ag nanoparticles owing to their strong surface plasmon resonance, broaden the light absorption range into the visible region and act as electron mediators to facilitate efficient charge separation in semiconductor-based photocatalysts [56]. Mechanistically, upon visible-light irradiation, LSPR excitation in Ag nanoparticles generates energetic (“hot”) electrons, which can be injected into the conduction band of the semiconductor. This process enhances electron density in the conduction band, promoting the formation of reactive oxygen species such as $O_2\cdot^-$. Simultaneously, improved charge separation increases hole availability for ·OH radical formation, thereby accelerating reaction kinetics. Primarily, during light irradiation, photogenerated electrons are transferred from the semiconductor

conduction band to Ag nanoparticles, which effectively suppresses electron-hole recombination and promotes the generation of reactive oxygen species (OH· and O_2·⁻). These radicals concurrently target the xanthene ring structure of RB and the azo linkage of AY, resulting in rapid cleavage of the chromophores and subsequent mineralization. The synergistic effect is particularly conspicuous within mixed dye systems, where increased ROS availability facilitates the simultaneous degradation of both dyes with greater efficiency than in single-dye systems. Particularly, the enhancement is attributed to (i) surface plasmon resonance (SPR)-induced visible-light absorption, (ii) formation of a Schottky junction facilitating electron trapping and suppressing charge recombination, and (iii) improved interfacial charge transfer [56].**Figure 6c** illustrates the schematic diagram of the photocatalytic degradation process. Moreover, silver nanoparticles enhance the catalytic stability and reusability of the system, underscoring their role in expediting degradation kinetics and achieving superior treatment outcomes for complex dye wastewater.

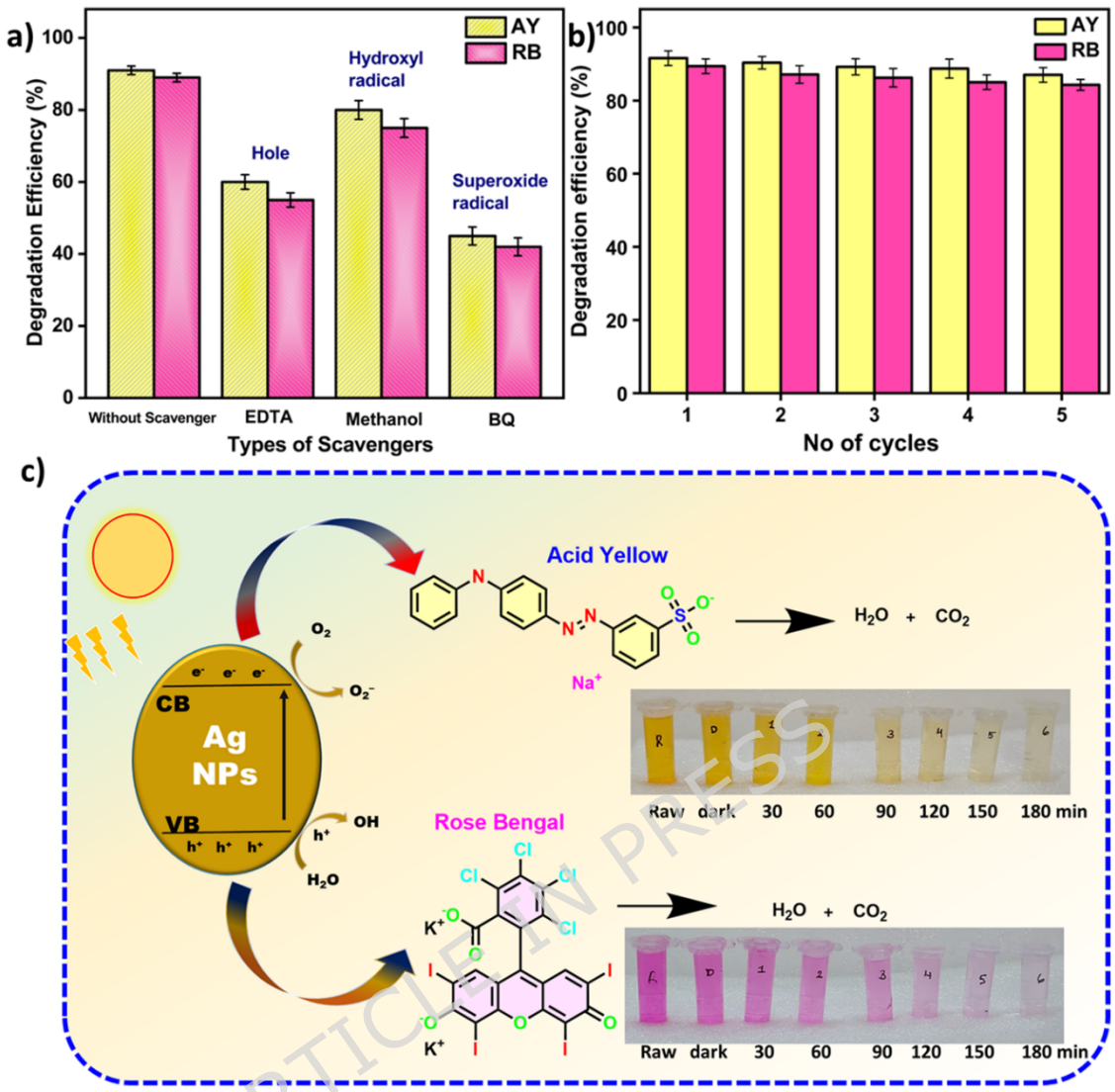

Figure 6: (a) Scavenger study, (b) Reusability results, and (c) Schematic diagram of photocatalytic degradation of AY and RB dyes using Ag NPs.

5. Conducting Ink Application of Ag NPs

Initially, a hydroxyethyl cellulose (HEC) binder solution was created by dissolving 0.2 wt% HEC in a 1:1 methanol-water mixture, stirred magnetically at 500-800 rpm for 120 minutes, producing a clear, viscous solution. Separately, 6 g of silver nanoparticles obtained through metal displacement were dispersed in 10 mL of ethanol and stirred at 800-1000 rpm at room temperature. Then, 2-3 mL of this HEC binder was added to the dispersion, which was stirred for an additional 160 minutes at 1000 rpm to promote proper interaction between the silver nanoparticles and

the polymer binder. The suspension was then ultrasonicated at high power for 2 hours to ensure a uniform dispersion suitable for conductive ink formulation. Afterwards, the ink was loaded into a plastic whiteboard marker cartridge and used to write on paper. The coated paper was dried in a vacuum oven at 80 °C for 60 minutes and then incorporated into an electrical circuit to assess its conductivity. The prepared track photos and corresponding conductivity are shown in **Figure 7(a)**. The conductivity measurement using a digital meter for the conducting tracks is shown in Supplementary Information (**SI) Video V1.**

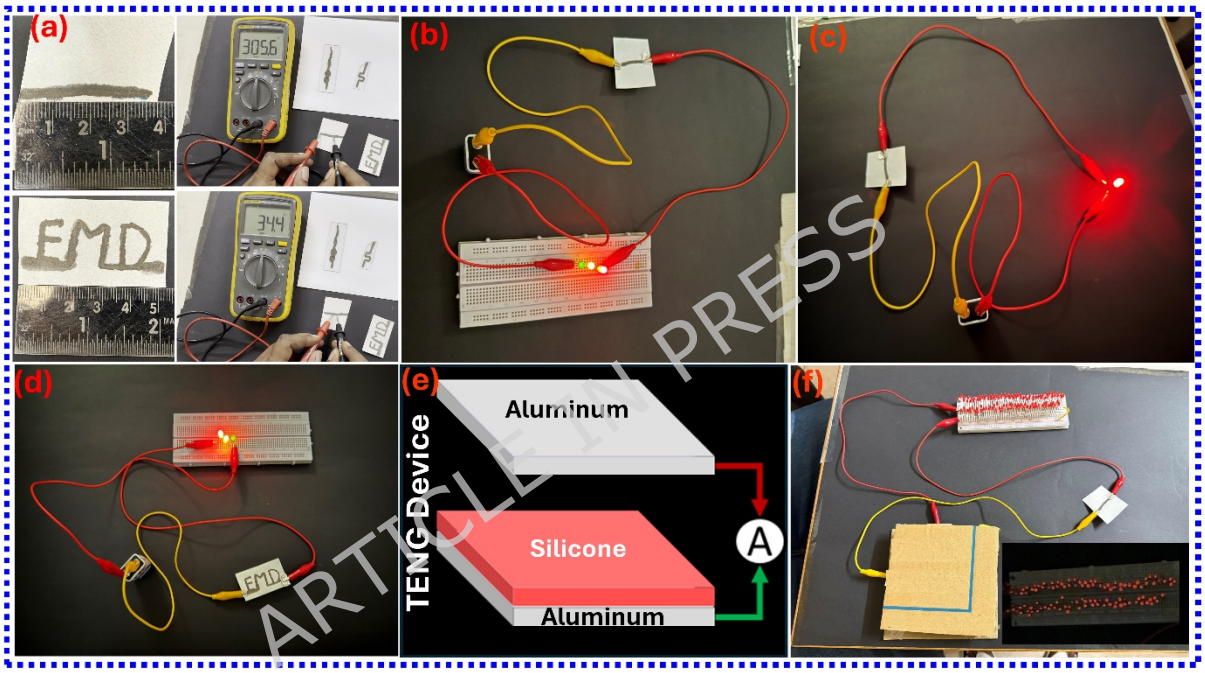

Figure 7: (a-b) An Ag NPs conducting ink path track, (c) A battery connection illuminating red LED, (d) A battery connection illuminating green, orange, and red LEDs, (e) A TENG device, and (f) A TENG device integrated conducting circuit, illuminating 240 series connected LEDs.

The conductive silver ink track was first evaluated using a standard 9 V battery and three different LED colors, green, orange, and red (shown in **Figure 7(b-d)**). The printed silver-ink pathways exhibited excellent electrical conductivity, successfully illuminating all LEDs with high brightness. Furthermore, when the conductive pattern was written in the form of the letters “EMD,” the combined set of LEDs also glowed uniformly, demonstrating the robustness and reliability of the printed

conductive tracks (shown in **Figure 7(d**). The conductive silver-ink tracks were further evaluated by replacing the 9 V battery with the output from a triboelectric nanogenerator (TENG) (**Figure 7e**). The TENG, composed of a silicone rubber-aluminium friction pair, was fabricated following our previously reported procedure, and its performance characteristics are detailed in an earlier publication [57]. Instead of individual LEDs, a series-connected LED array was used to assess the current-carrying capability of the printed pathways (**Figure 7f**). The Ag-ink circuits demonstrated excellent conductivity, enabling the TENG output to drive the entire LED series with bright and uniform illumination. The corresponding video showing the illumination of 240 LEDs is provided in the Supplementary Information (**SI) Video V2.**

Conclusions

The present study demonstrates a simple and effective Mg–tartaric acid-assisted metal-displacement route for synthesizing well-dispersed, oxidation-resistant Ag nanoparticles. The synergistic roles of magnesium as a reductant and tartaric acid as a stabilizing/capping agent enabled rapid room-temperature formation of uniform Ag NPs. Comprehensive structural and optical analyses confirmed their high crystallinity, purity, and plasmonic stability. These nanoparticles showed strong visible-light photocatalytic activity, degrading Acid Yellow and Rose Bengal by 91.6% and 89.4%, respectively, following first-order kinetics and maintaining stability across multiple reuse cycles. The Ag NPs were further formulated into a conductive ink that produced efficient printed pathways capable of operating in a self-powered configuration when coupled with a triboelectric nanogenerator, successfully illuminating a 240-LED series under biomechanical input. Overall, this scalable and environmentally benign approach delivers multifunctional Ag NPs suitable for photocatalysis and printed electronics.

Author contributions: RKK: Investigation, Methodology, Data curation, Formal analysis, Writing - original draft. **RK:** Investigation, Methodology, Data curation, Formal analysis, **NM:** Investigation, Methodology, Formal

analysis, **NV:** Investigation, Methodology, Formal analysis, **RN:** Investigation, Methodology, Formal analysis, **RKR:** Formal analysis, Funding acquisition, Methodology, Resources, Supervision, Validation, Visualization, Writing - review & editing. **HD:** Formal analysis, Funding acquisition, Methodology, Resources, Supervision, Validation, Visualization, Writing - review & editing. **CRM:** Conceptualization, Data curation, Formal analysis, Project administration, Resources, Software, Validation, Visualization, Writing - original draft, Writing - review & editing, **MD:** Conceptualization, Data curation, Formal analysis, Project administration, Resources, Software, Validation, Visualization, Writing - original draft, Writing - review & editing, **GM:** Investigation, Methodology, Formal analysis, Data curation, Writing - original draft, **UKK:** Conceptualization, Data curation, Formal analysis, Funding acquisition, Methodology, Project administration, Resources, Supervision, Validation, Visualization, Writing - original draft, Writing - review & editing.

Data Availability: The datasets generated or analysed during this study are available from the corresponding author upon reasonable request.

Conflicts of interest: There are no conflicts to declare.

Funding: No, this research did not receive funding

Supporting information

Video V1: Conductivity test for Ag ink pattern tracks

Video V2: A TENG device integrated conductivity tracks powering 240 series connected LEDs.

Reference:

1. Zhang, Q., Li, N., Goebl, J., Lu, Z. & Yin, Y. A Systematic Study of the Synthesis of Silver Nanoplates: Is Citrate a “Magic” Reagent? *J Am Chem Soc* 133, 18931–18939 (2011).

2. Muthukrishnan, S., Bhakya, S. & Ramalingam, V. Metal nanoparticles synthesis: an overview of different synthesis methods, mode of action and their biomedical application. *Discover Applied Sciences* 7, 1079 (2025).

3. Chandak, V. S. & Nagime, P. V. Synthesis, characterization and applications of silver nanoparticles (Ag-NPs) in the field of electronics and optoelectronics device- A review. *Hybrid Advances* 8, 100389 (2025).

4. Hosny, S. *et al.* A Comprehensive Review of Silver Nanoparticles (AgNPs): Synthesis Strategies, Toxicity Concerns, Biomedical Applications, AI-Driven Advancements, Challenges, and Future Perspectives. *Arab J Sci Eng* 1–48 (2025) doi:10.1007/s13369-025-10612-0.

5. Hong, G. B. *et al.* Facile Synthesis of Silver Nanoparticles and Preparation of Conductive Ink. *Nanomaterials* 12, 171 (2022).

6. Sati, A., Ranade, T. N., Mali, S. N., Ahmad Yasin, H. K. & Pratap, A. Silver Nanoparticles (AgNPs): Comprehensive Insights into Bio/Synthesis, Key Influencing Factors, Multifaceted Applications, and Toxicity–A 2024 Update. *ACS Omega* 10, 7549–7582 (2025).

7. Fahim, M. *et al.* Green synthesis of silver nanoparticles: A comprehensive review of methods, influencing factors, and applications. *JCIS Open* 16, 100125 (2024).

8. Sati, A. *et al.* From Past to Present: Gold Nanoparticles (AuNPs) in Daily Life–Synthesis Mechanisms, Influencing Factors, Characterization, Toxicity, and Emerging Applications in Biomedicine, Nanoelectronics, and Materials Science. *ACS Omega* 10, 33999–34087 (2025).

9. Kimling, J. *et al.* Turkevich Method for Gold Nanoparticle Synthesis Revisited. *J Phys Chem B* 110, 15700–15707 (2006).

10. Umar, A. *et al.* Modification of silver nanoparticles (AgNPs) with tollens reagent for selective colorimetric detection of formaldehyde. *Results Chem* 17, 102586 (2025).

11. Halder, S., Ahmed, A. N., Gafur, Md. A., Seong, G. & Hossain, M. Z. Size-Controlled Facile Synthesis of Silver Nanoparticles by Chemical Reduction Method and Analysis of Their Antibacterial Performance. *ChemistrySelect* 6, 9714–9720 (2021).

12. Ahmed, S., Ahmad, M., Swami, B. L. & Ikram, S. A review on plants extract mediated synthesis of silver nanoparticles for antimicrobial applications: A green expertise. *J Adv Res* 7, 17–28 (2016).

13. Alam, Md. N. Green Sonochemical Synthesis of Gold Nanoparticles by Carbazole and Sensing of ct-DNA. *Chemistry Africa* 8, 2045–2054 (2025).

14. Gul, M., Kashif, M., Muhammad, S., Azizi, S. & Sun, H. Various Methods of Synthesis and Applications of Gold-Based Nanomaterials: A Detailed Review. *Cryst Growth Des* 25, 2227–2266 (2025).

15. Sulistyani, Santosa, S. J., Roto, Louise, I. S. Y. & Tahir, I. Green electrochemical synthesis of ultra-small and highly stable silver

nanoparticles in an electrolyte solution of polyethylene glycol-1000. *Case Studies in Chemical and Environmental Engineering* 11, 101214 (2025).

16. Khaydarov, R. A., Khaydarov, R. R., Gapurova, O., Estrin, Y. & Scheper, T. Electrochemical method for the synthesis of silver nanoparticles. *Journal of Nanoparticle Research* 11, 1193–1200 (2009).

17. Cheng, H., Wang, C., Qin, D. & Xia, Y. Galvanic Replacement Synthesis of Metal Nanostructures: Bridging the Gap between Chemical and Electrochemical Approaches. *Acc Chem Res* 56, 900–909 (2023).

18. Kong, X. *et al.* Galvanic Replacement Reaction: Enabling the Creation of Active Catalytic Structures. *ACS Appl Mater Interfaces* 15, 41205–41223 (2023).

19. Kandikonda, R. *et al.* Redox-driven synthesis of stable copper nanoparticles *via* metal displacement and their application in organic dye degradation. *Mater Adv* 6, 9575–9589 (2025).

20. Zozulya, G., Kuntyi, O., Mnykh, R., Kytsya, A. & Bazylyak, L. Synthesis of silver nanoparticles by sonogalvanic replacement on aluminium powder in sodium polyacrylate solutions. *Ultrason Sonochem* 84, 105951 (2022).

21. Kumar, S. *et al.* Extraction of Metallic Nanoparticles from Electronic Waste for Biomedical Applications: Pioneering Sustainable Technological Progress. *Sustainability* 17, 2100 (2025).

22. Mondal, M. S., Paul, A. & Rhaman, M. Recycling of silver nanoparticles from electronic waste via green synthesis and application of AgNPs-chitosan based nanocomposite on textile material. *Sci Rep* 13, 13798 (2023).

23. Himanshi *et al.* Advances in magnesium spinel ferrites for photocatalytic degradation of methylene blue: Challenges and future prospectives. *Journal of Magnesium and Alloys* https://doi.org/10.1016/j.jma.2025.10.021 (2025) doi:10.1016/j.jma.2025.10.021.

24. Durmazel, S., Üzer, A., Erbil, B., Sayın, B. & Apak, R. Silver Nanoparticle Formation-Based Colorimetric Determination of Reducing Sugars in Food Extracts via Tollens' Reagent. *ACS Omega* 4, 7596–7604 (2019).

25. Gandlevskiy, N. *et al.* Ultrasound-assisted green synthesis of silver nanoparticles using Ruta graveolens L. Extract and antitumor evaluation. *Ultrason Sonochem* 117, 107340 (2025).

26. Šimonová, Z. *et al.* The Effects of Nature-Inspired Synthesis on Silver Nanoparticle Generation. *ACS Omega* 7, 4850–4858 (2022).

27. Jadhav, S. D., Patil, V. S., Maneri, M. I. & Mahale, M. K. Photo-Degradation of Acid Yellow 36 Dye Using ZnFe2O4 as a Photocatalyst. *Russian Journal of Applied Chemistry* 98, 153–159 (2025).

28. Sharma, B. *et al.* Rose Bengal as a multifunctional agent: from biomedical uses to catalysis and materials science. *Coord Chem Rev* 550, 217413 (2026).

29. Alagarsamy, V. *et al.* NiS-ZnS quantum dots as visible-light photocatalysts for enhanced dye degradation in sustainable wastewater treatment. *Chemical Physics Impact* 11, 100912 (2025).

30. Singaravelan, R. & Bangaru Sudarsan Alwar, S. Electrochemical synthesis, characterisation and phytogenic properties of silver nanoparticles. *Applied Nanoscience 2015 5:8* 5, 983–991 (2015).

31. Ali, Md. H. *et al.* Analysis of Crystallographic Structures and Properties of Silver Nanoparticles Synthesized Using PKL Extract and Nanoscale Characterization Techniques. *ACS Omega* 8, 28133–28142 (2023).

32. Maheshkumar, B. *et al.* Synthesis and characterization of silver nanoparticles for photocatalytic application. *Hybrid Advances* 10, 100417 (2025).

33. Liu, C. *et al.* Synthesis of Clean Cabbagelike (111) Faceted Silver Crystals for Efficient Surface-Enhanced Raman Scattering Sensing of Papaverine. *Anal Chem* 90, 9805–9812 (2018).

34. Zhang, Z. *et al.* pH-controlled growth of triangular silver nanoprisms on a large scale. *Nanoscale Adv* 1, 4904–4908 (2019).

35. Joshi, N. *et al.* Biosynthesis of silver nanoparticles using Carissa carandas berries and its potential antibacterial activities. *J Solgel Sci Technol* 86, 682–689 (2018).

36. Lai, C. H. *et al.* Near infrared surface-enhanced Raman scattering based on star-shaped gold/silver nanoparticles and hyperbolic metamaterial. *Scientific Reports 2017 7:1* 7, 1–8 (2017).

37. Pilot, R. & Massari, M. Silver nanoparticle aggregates: Wavelength dependence of their SERS properties in the first transparency window of biological tissues. *Chemical Physics Impact* 2, 100014 (2021).

38. Manna, A., Imae, T., Aoi, K., Okada, M. & Yogo, T. Synthesis of Dendrimer-Passivated Noble Metal Nanoparticles in a Polar Medium: Comparison of Size between Silver and Gold Particles. *Chemistry of Materials* 13, 1674–1681 (2001).

39. Henglein, A. Physicochemical properties of small metal particles in solution: 'microelectrode' reactions, chemisorption, composite metal particles, and the atom-to-metal transition. *J Phys Chem* 97, 5457–5471 (1993).

40. Kolwas, K. & Derkachova, A. Impact of the Interband Transitions in Gold and Silver on the Dynamics of Propagating and Localized Surface Plasmons. *Nanomaterials* 10, 1411 (2020).

41. Sun, X., Dong, S. & Wang, E. One-Step Preparation and Characterization of Poly(propyleneimine) Dendrimer-Protected Silver Nanoclusters. *Macromolecules* 37, 7105–7108 (2004).

42. Varghese Alex, K. *et al.* Green Synthesized Ag Nanoparticles for Bio-Sensing and Photocatalytic Applications. *ACS Omega* 5, 13123–13129 (2020).

43. Bala, S. & Mondal, R. Gel–based Controlled Synthesis of Silver Nanoparticles and Their Applications in Catalysis, Sensing and Environmental Remediation. *ChemistrySelect* 2, 389–398 (2017).

44. Talabani, R. F., Hamad, S. M., Barzinjy, A. A. & Demir, U. Biosynthesis of Silver Nanoparticles and Their Applications in Harvesting Sunlight for Solar Thermal Generation. *Nanomaterials* 11, 2421 (2021).

45. Pasieczna-Patkowska, S. *et al.* Application of Fourier Transform Infrared (FTIR) Spectroscopy in Characterization of Green Synthesized Nanoparticles. *Molecules 2025, Vol. 30,* 30, (2025).

46. Begum, I. *et al.* A Combinatorial Approach towards Antibacterial and Antioxidant Activity Using Tartaric Acid Capped Silver Nanoparticles. *Processes* 10, 716 (2022).

47. Bogale, B. L. *et al.* Green and facile synthesis of silver nanoparticles (Ag NPs) using Rhamnus prinoides (Gesho) leaf extract for antibacterial, antioxidant and photocatalytic activities. *Next Nanotechnology* 7, 100163 (2025).

48. Jyoti, K., Baunthiyal, M. & Singh, A. Characterization of silver nanoparticles synthesized using Urtica dioica Linn. leaves and their synergistic effects with antibiotics. *J Radiat Res Appl Sci* 9, 217–227 (2016).

49. Jahan Tamanna, N., Sahadat Hossain, Md., Mohammed Bahadur, N. & Ahmed, S. Green synthesis of Ag2O & facile synthesis of ZnO and characterization using FTIR, bandgap energy & XRD (Scherrer equation, Williamson-Hall, size-train plot, Monshi- Scherrer model). *Results Chem* 7, 101313 (2024).

50. Martínez-Higuera, A. *et al.* Hydrogel with silver nanoparticles synthesized by Mimosa tenuiflora for second-degree burns treatment. *Sci Rep* 11, 11312 (2021).

51. Ghodake, G. *et al.* Whey peptide-encapsulated silver nanoparticles as a colorimetric and spectrophotometric probe for palladium(II). *Microchimica Acta 2019 186:12* 186, 1–9 (2019).

52. Kundu, S., Wang, Y., Xia, W. & Muhler, M. Thermal Stability and Reducibility of Oxygen-Containing Functional Groups on Multiwalled Carbon Nanotube Surfaces: A Quantitative High-Resolution XPS and TPD/TPR Study. *Journal of Physical Chemistry C* 112, 16869–16878 (2008).

53. Vasil'kov, A., Batsalova, T., Dzhambazov, B. & Naumkin, A. XPS study of silver and copper nanoparticles demonstrated selective anticancer, proapoptotic, and antibacterial properties. *Surface and Interface Analysis* 54, 189–202 (2022).

54. Boronin, A. I., Koscheev, S. V. & Zhidomirov, G. M. XPS and UPS study of oxygen states on silver. *J Electron Spectros Relat Phenomena* 96, 43–51 (1998).

55. Murugadoss, G., Kumar, D. D., Kumar, M. R., Venkatesh, N. & Sakthivel, P. Silver decorated CeO2 nanoparticles for rapid photocatalytic degradation of textile rose bengal dye. *Sci Rep* 11, 1–13 (2021).

56. Mandal, K. *et al.* Spectroscopic approach to optimize the biogenic silver nanoparticles for photocatalytic removal of ternary dye mixture and ecotoxicological impact of treated wastewater. *Sci Rep* 14, 31174 (2024).

57. Madathil, N. *et al.* Enhancing Triboelectric Nanogenerators Performance with MXene–Silicone Nanocomposites: A Leap Forward in Energy Harvesting and Touch-Sensitive Technologies. *ACS Appl Electron Mater* 6, 5574 (2024).

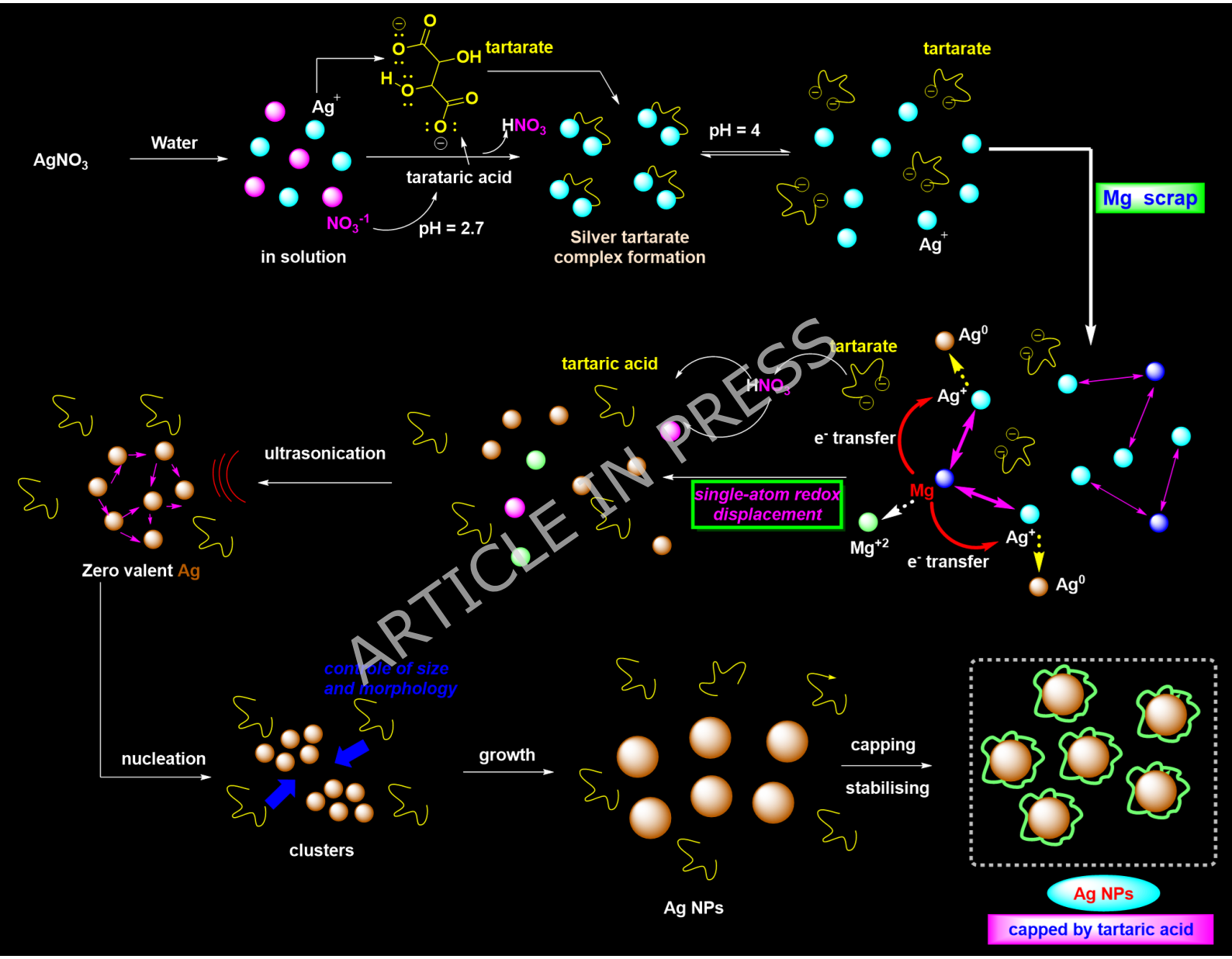

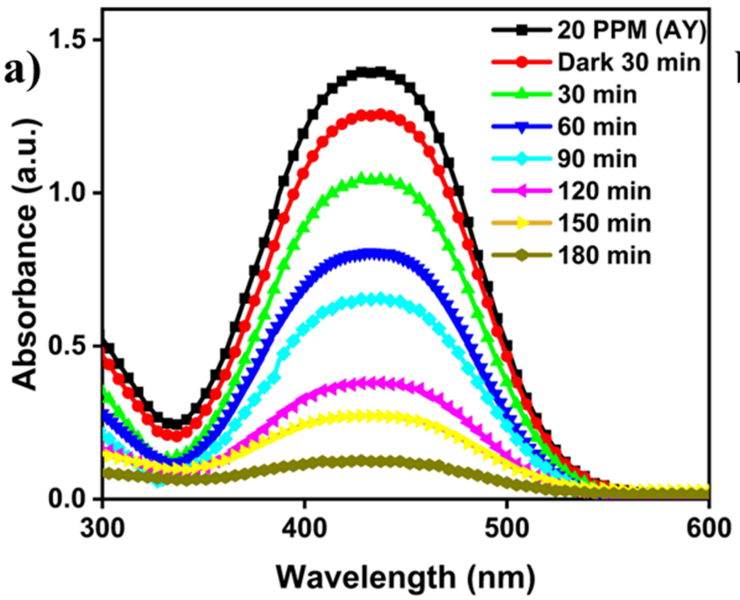

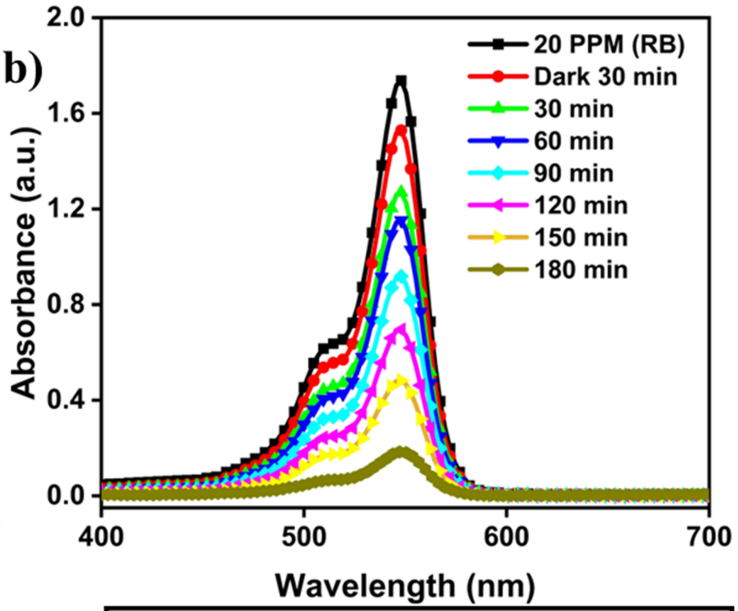

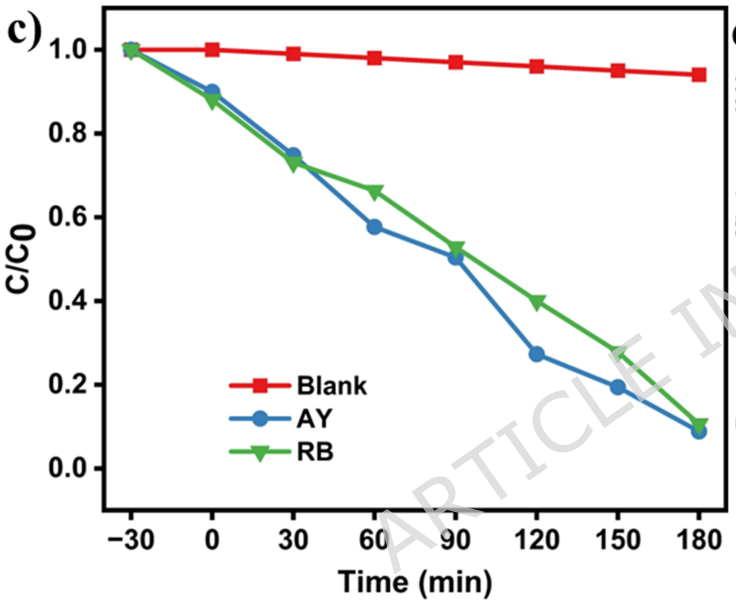

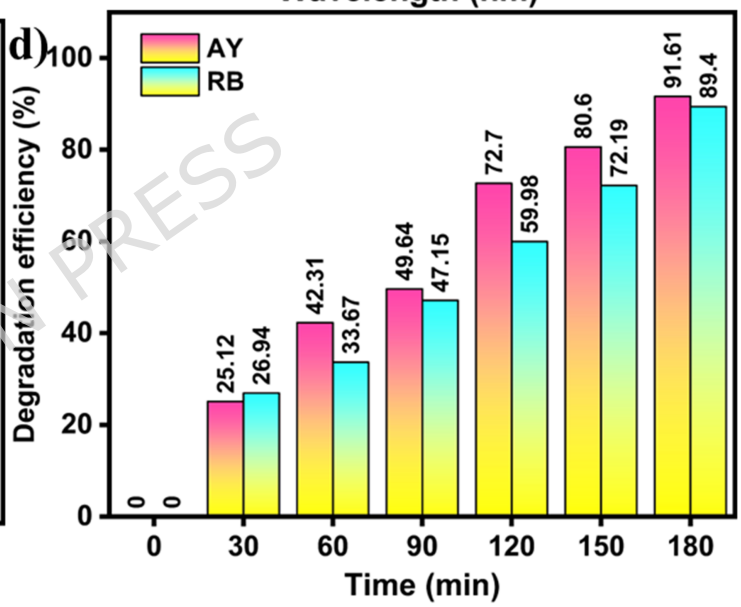

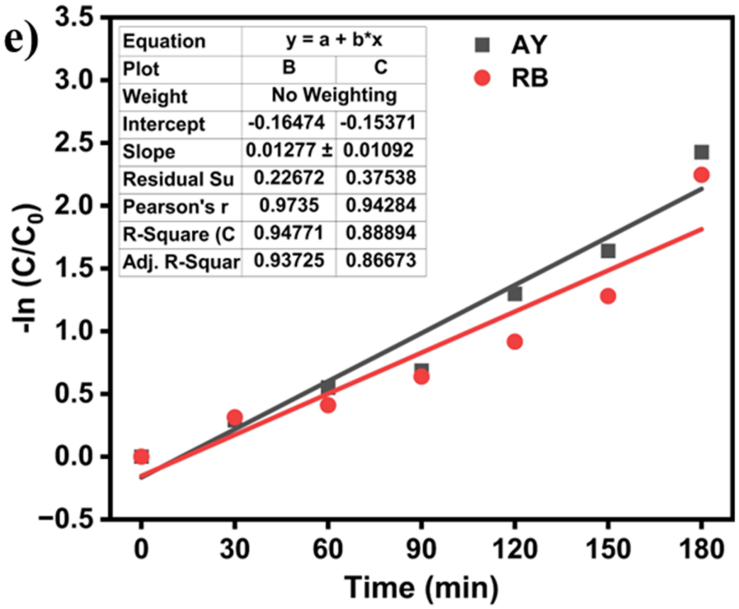

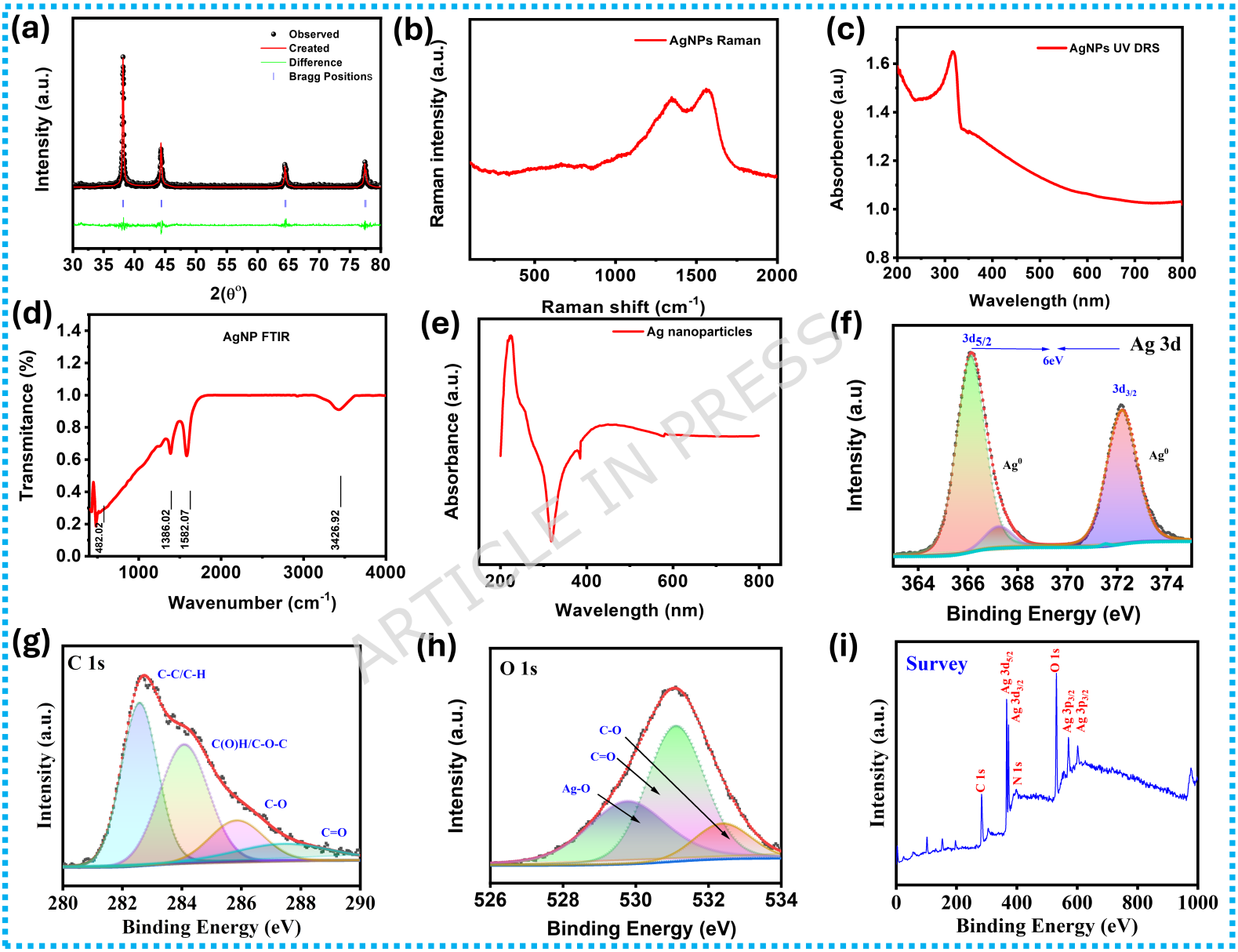

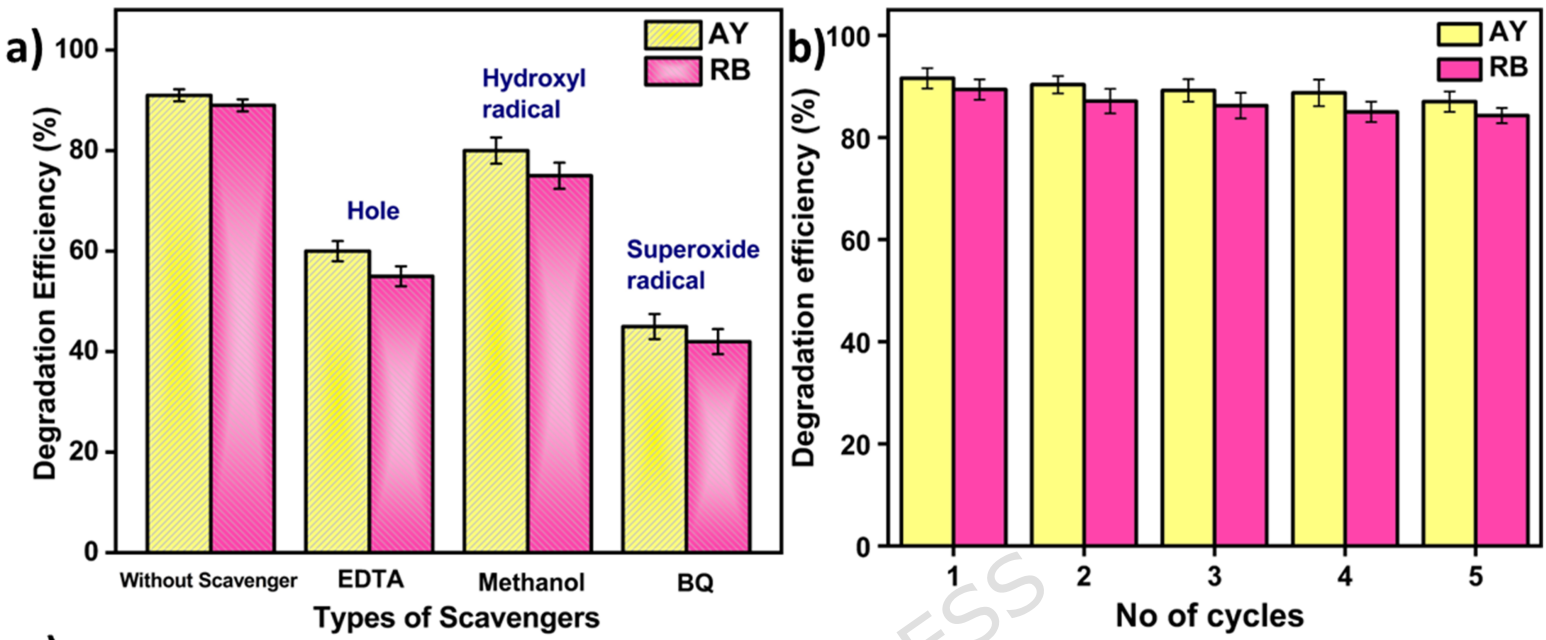

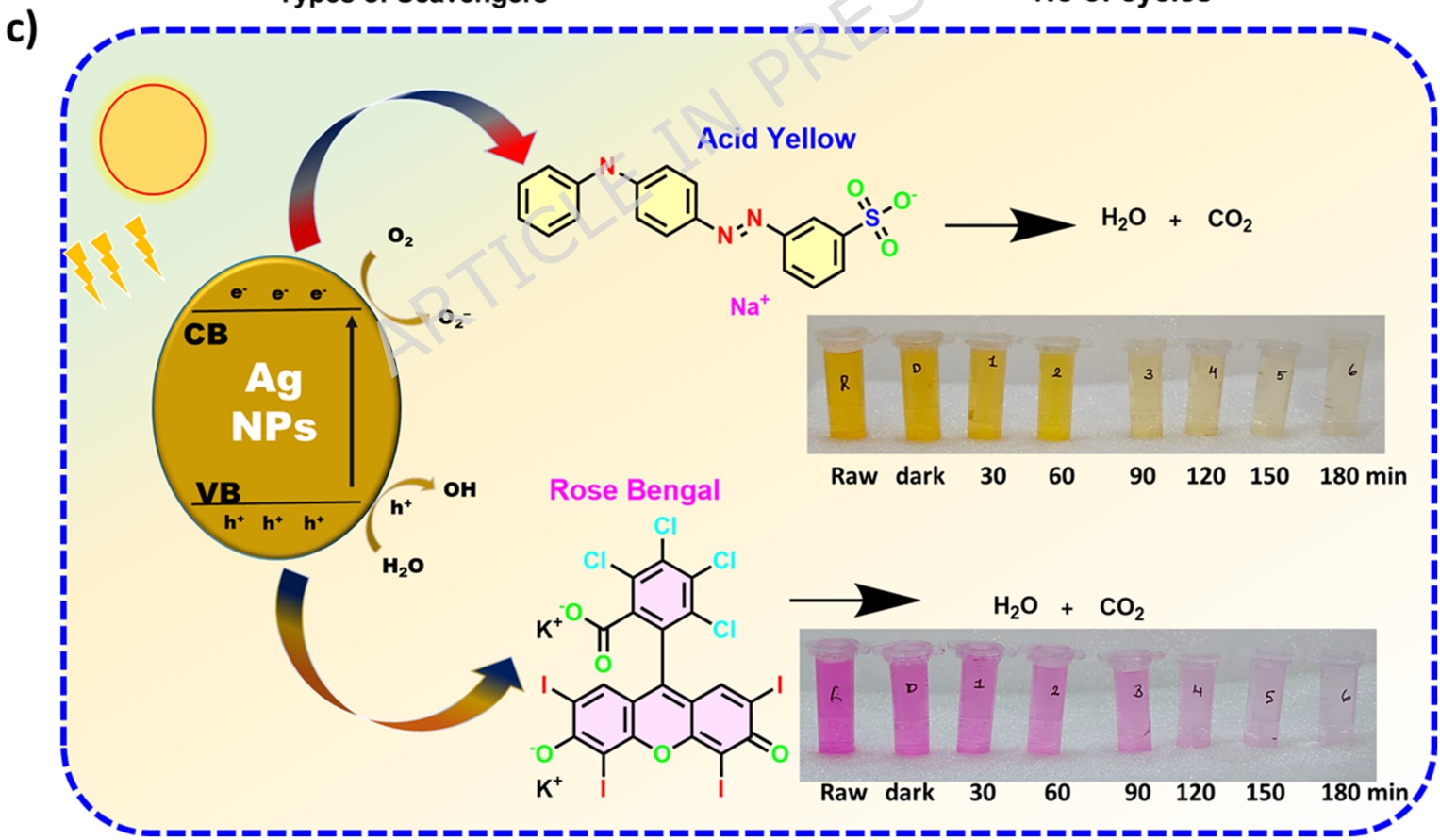

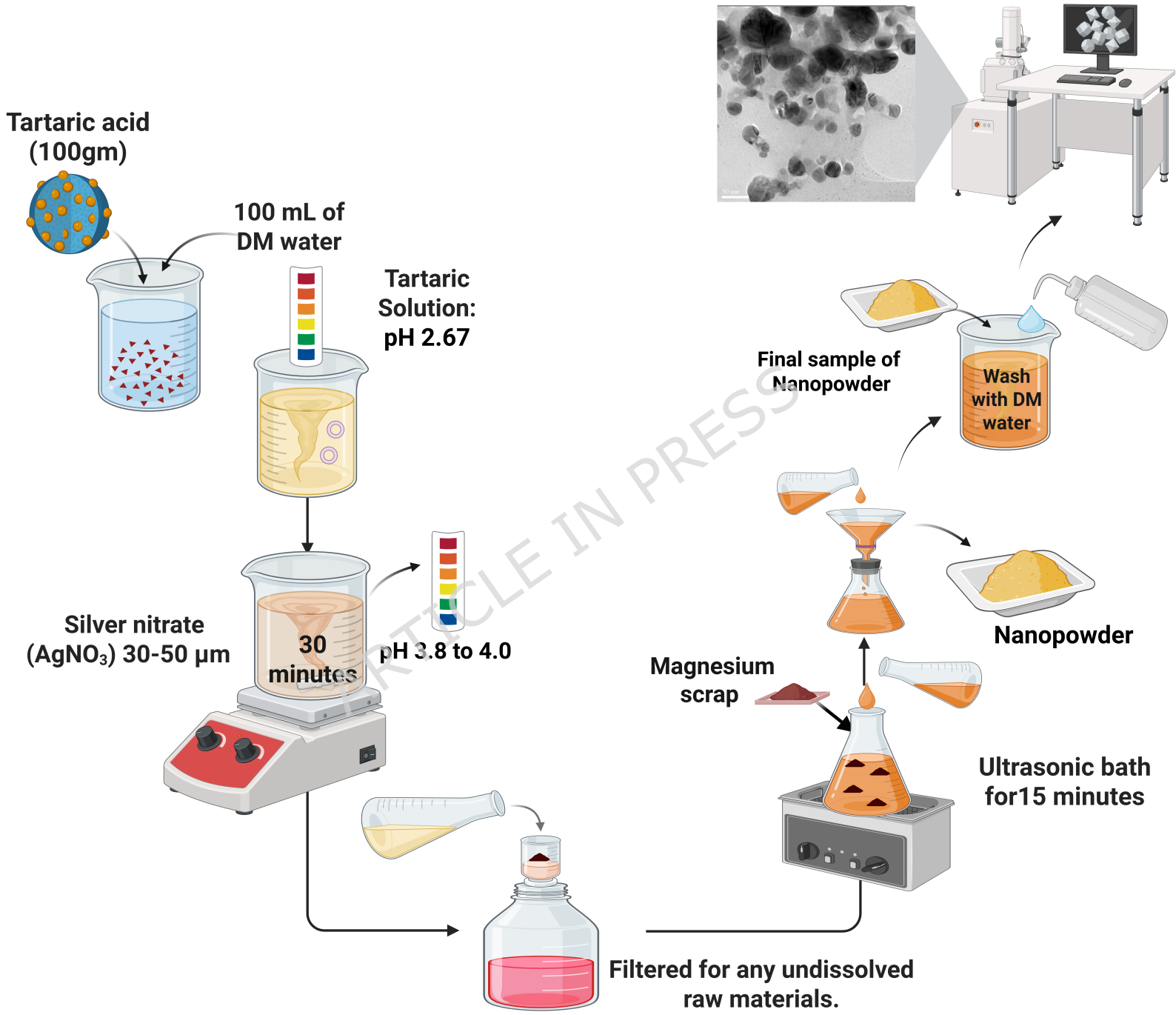

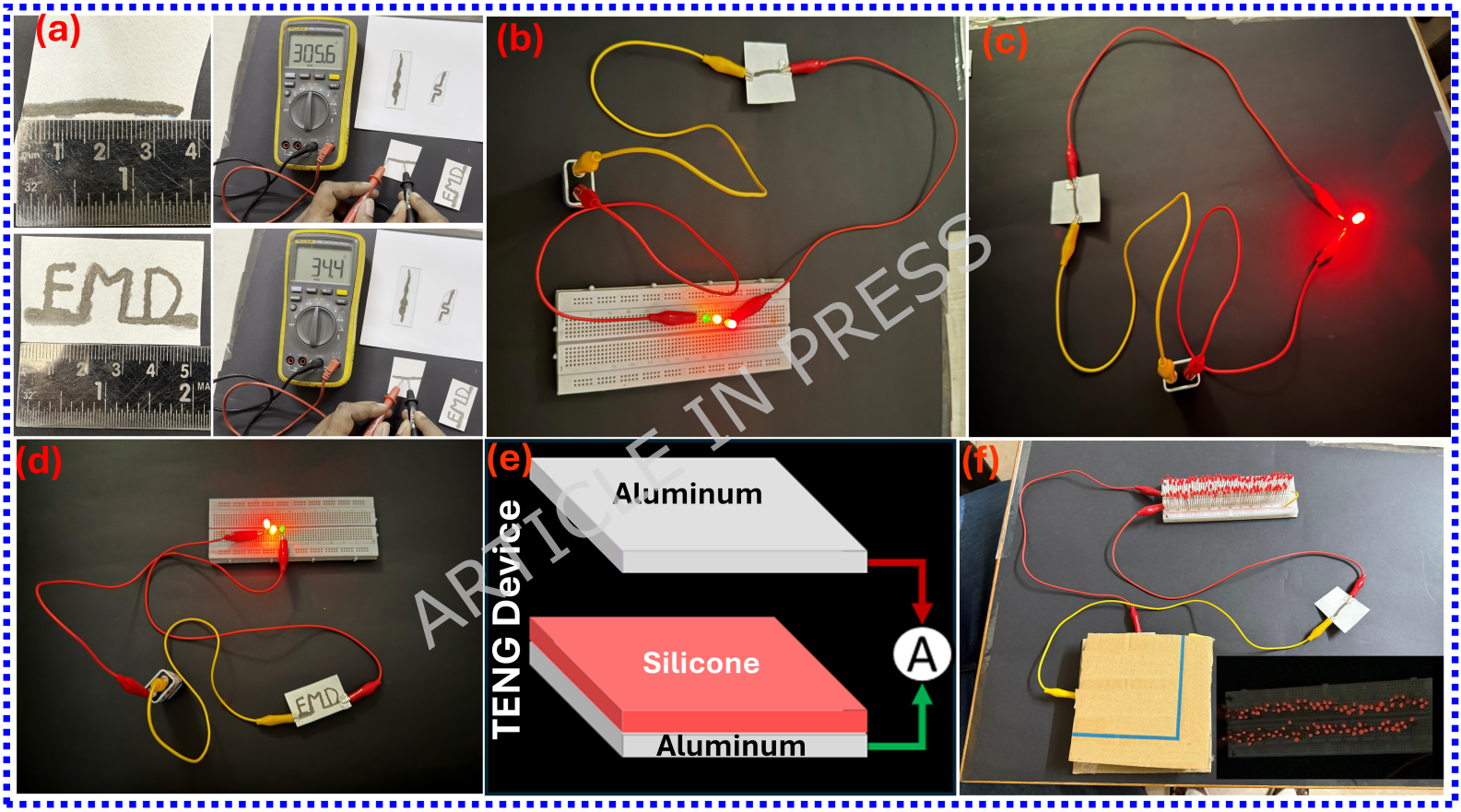

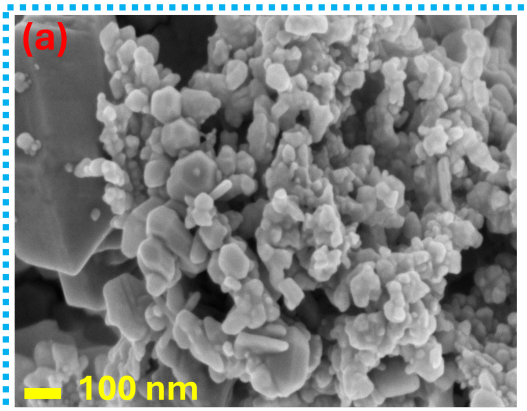

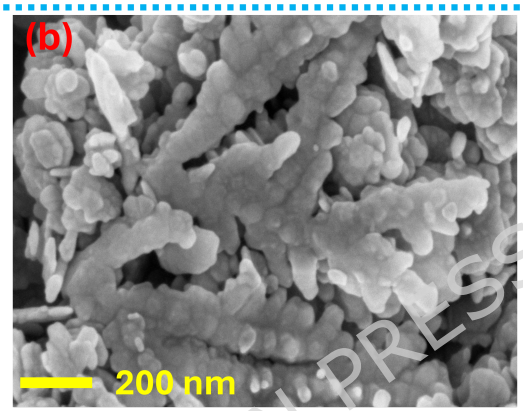

(c)

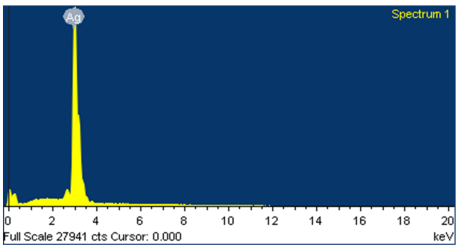

Element	Weight%	Atomic%
Ag L	100.00	100.00
Totals	100.00